RSC Advances

PAPER

View Article Online
View Journal | View Issue

Cite this: RSC Adv., 2016, 6, 67898

Nitrogen-doped reduced graphene oxide and aniline based redox additive electrolyte for a flexible supercapacitor†

K. Vijaya Sankar,[a] R. Kalai Selvan,*[a] R. Hari Vignesh[b] and Y. S. Lee*[b]

Received 4th May 2016
Accepted 4th July 2016

DOI: 10.1039/c6ra11521g

www.rsc.org/advances

Nitrogen-doped reduced graphene oxide (N-rGO) with a layered structure was prepared by a simple hydrothermal method. Structural and elemental analysis revealed the successful doping of N atoms into the carbon sites of graphene. The presence of wrinkles and folds in the transmission electron microscope images provided evidence for the excellent flexibility of the prepared N-rGO. Additionally, the curved edges further illustrated the implantation of N atoms in the carbon sites of graphene. The unreduced oxygen functional groups and N atoms provided additional pseudocapacitance to the N-rGO. The flexible N-rGO fiber supercapacitor exhibited a 5.7 times higher specific capacitance with the aniline additive than without the additive. The maximum specific capacitance was 2.02 F m^{-1} at 5 mV s^{-1}. Finally, a serially connected device was integrated with a commercially available solar cell and used to power a light emitting diode in different flexible modes, after charging up to 2.2 V. All these results demonstrate that the fabricated device can be a suitable energy storage device for various flexible energy storage applications.

1. Introduction

Flexible electronic devices, including displays, implantable medical devices, and bendable smart phones, have created new revolutions in the electronic industry. However, their flexibility depends on the energy storage device. Thus, the research community is under pressure to fabricate flexible energy storage devices. The device flexibility is determined by the appropriate choice of current collector and electrolyte. Fiber-based current collectors are better than planar electrodes because of their high flexibility and small size. Polymer gel electrolytes have many advantages over aqueous electrolytes: there are no packaging problems, they do not leak, and they do not require separators. Polymer gel electrolytes also offer improved safety, a reduction of the internal resistance, flexibility, easy device integration, environmental stability, and a low weight.[1–4]

Batteries, supercapacitors (SCs), and conventional capacitors (CCs) are the existing energy storage devices on the market for multifunctional applications. In the near future, SCs will likely occupy a foremost place in energy storage devices due to their excellent cycling stability, higher power density than batteries, higher energy density than CCs, good safety record, lack of memory effects, low cost, and good rate capability. However, SCs store only a finite quantity of energy compared to batteries. The challenge is to improve the energy density of SCs without losing their excellent power density (the energy density mainly depends on the specific capacitance and the square of the working potential window).

SCs can be categorized into three types based on their charge storage mechanism and electrode configuration: (i) pseudocapacitor (PC), (ii) electric double-layer capacitor (EDLC), and (iii) hybrid supercapacitor (HC). The charge storage mechanism of PCs occurs by a surface redox reaction or by a charge transfer reaction. PCs deliver a high energy density and a high specific capacitance but have less cycling life due to the irreversibility of the redox reaction, material degradation, volume expansion, and phase transformation. So far, conducting polymers and transition metal oxides (sulfides, hydroxides) have been explored as electrode materials in PCs. EDLCs store the charges through non-faradaic reactions or by the formation of an electric double layer at the electrode/electrolyte interface. They show an excellent life cycle, high power density, good electronic conductivity, ideal capacitive behavior, no phase change, and are easy to fabricate. However, EDLCs lack energy density. Various carbon-based nanostructured electrode materials were investigated for use in EDLCs. Similarly, the HC stores the charge by both faradaic and non-faradaic electrochemical reactions at the electrode/electrolyte interface. HCs possess a high energy density, high potential window, good cycle life, and good specific capacitance. However, the mass and charge balance between the positive and negative electrodes is important to achieve excellent electrochemical performances from HCs.

EDLCs are considered as ideal energy storage devices for futuristic applications.[5–7] The energy density of EDLCs may be

[a]Solid State Ionics and Energy Devices Laboratory, Department of Physics, Bharathiar University, Coimbatore – 641 046, Tamil Nadu, India. E-mail: selvankram@gmail.com; Fax: +91 422 2425706

[b]Faculty of Applied Chemical Engineering, Chonnam National University, Gwangju 500-757, Korea. E-mail: yslee@chonnam.ac.kr

† Electronic supplementary information (ESI) available. See DOI: 10.1039/c6ra11521g

improved by using carbonaceous electrode materials, *e.g.*, activated carbon, carbon nanotubes, carbon aerogels, and graphene.[7] Among these, graphene is one of the best electrode materials due to its many fascinating properties (*e.g.*, high electronic conductivity, high tensile strength, good flexibility, optical transparency, chemical stability, high surface area, and high theoretical specific capacitance).[8–10] However, the main drawback of graphene sheets is the re-stacking problem that occurs from strong van der Waals attractions. One solution is to use pseudocapacitive and electric double layer materials as spacers to reduce the re-stacking problem.[9,11–13]

Recently, the doping of heteroatoms (N, B, S, and P) has emerged as a remedy to overcome the re-stacking problem because it also improves the wettability and provides an additional pseudocapacitance. Among the reported heteroatoms, N is superior due to its electron donor properties (the presence of five valence electrons attracts more protons and generates a pseudocapacitance).[14,15] Various methods have been adapted to synthesize heteroatom-doped graphene, such as chemical vapor deposition, thermal treatments, plasma treatments, ball milling, arc-discharge, and wet chemical methods.[12] Of these methods, the wet chemical method is superior due to its low cost, low reaction temperature, ease of synthesis, mass sample production from solution-based precursors, and ease of heteroatom doping.[12] Similarly, the electrochemical performance of the device can be further improved by using redox additive electrolytes. Here, the redox additive is adsorbed on the active electrodes and undergoes redox reactions at particular potentials, which provide additional pseudocapacitance to the device. Various redox additives were used for SCs.[9] Aniline was chosen as the redox additive due to its high electronic conductivity, low cost, high flexibility, and number of oxidation states.[13]

Here, the objective is to fabricate N-doped rGO-based flexible fiber SCs. The N-doped reduced graphene oxide (N-rGO) was prepared by a simple hydrothermal method and acid-treated melamine (ATM) was used as the N source. Subsequently, to improve the electrochemical performance of the device, different amounts of aniline were used as a redox additive in the polymer gel (polyvinyl alcohol (PVA) + H_2SO_4) electrolyte. Here, for the first time, aniline used as redox additive and identified the optimum concentration for the better performance. The fabricated symmetric (N-rGO‖PVA + H_2SO_4 + aniline‖N-rGO) flexible fiber SC exhibited an excellent electrochemical performances. The aniline used device provided 5.7 times higher length capacitance than (N-rGO|PVA + H_2SO_4|N-rGO) device. Finally, the fabricated device was integrated with commercial solar cells (CSCs) at different conditions (normal, spiral, zigzag, and ring modes) to test the real-time applications.

2. Experimental methods and materials

2.1. Preparation of acid-treated melamine

Melamine (1 g) was dissolved (with stirring) in ethanol (20 mL) to create a saturated solution. After a few minutes, HNO_3 (0.2 M, 60 mL) was added to the solution with vigorous stirring that continued for 10 min. Finally, the sample (ATM) was washed with ethanol and dried at 60 °C overnight.

2.2. Preparation of N-doped reduced graphene oxide

The synthesis of graphene oxide (GO) was previously reported.[10,11] GO (40 mg) was dispersed in doubly distilled water (40 mL). Separately, ATM (10 mg) was dissolved in distilled water (5 mL) and added dropwise into the GO solution with stirring. After a 2 h, the solution was transferred to a Teflon-lined autoclave and placed in a muffle furnace at 180 °C overnight. When the reaction was complete, the autoclave was cooled to room temperature. The final product was washed with distilled water and dried at 80 °C overnight. The same procedure was used to prepare rGO, but without the use of ATM.

2.3. Characterization of materials

The phase purity and compound formation were examined using X-ray diffraction (XRD, Bruker D8 ADVANCE) with Cu Kα radiation. Fourier transform infrared spectroscopy (FT-IR, Bruker Tensor 27) was used to determine the presence of oxygen functional groups and the doping of N heteroatoms. The sample defects were characterized using Raman microscopy (Renishaw inVia Raman Microscope, He–Ne laser: 633 nm, 18 mW). The morphological features of the samples were analyzed using high-resolution transmission electron microscopy (HRTEM, JEOL JEM-2100). Further, elemental analysis was performed using X-ray photoelectron spectroscopy (XPS, Thermo Scientific MultiLab 2000).

2.4. Electrode and flexible fiber supercapacitor fabrication

N-rGO, carbon black, and polyvinylidene difluoride were mixed at a ratio of 80 : 15 : 5 using in *N*-methyl-2-pyrrolidine solution (0.4 mL). The mixture was ground for one hour to create homogeneous slurry. Then, stainless steel fibers (length = 6 cm) were dipped into the slurry and dried at 60 °C for overnight in a hot air oven. The measured active material loading was 2 mg.

The device was prepared using a polymer gel electrolyte. Initially, polyvinyl alcohol (PVA, 0.5 g) was added to 30 mL of hot water with stirring until a clear solution was achieved. Then, H_2SO_4 (1 M, 10 mL) was added dropwise with vigorous stirring. The polymer gel electrolyte was stirred until the solution level reached 10 mL. This electrolyte was named PAH000. The same procedure was adopted to prepare a polymer gel electrolyte with different amounts of the aniline redox additive (0.025 mL, 0.050 mL, 0.075 mL, and 0.100 mL). The electrolytes were named PAH025, PAH050, PAH075, and PAH100, respectively. Finally, the fiber electrode was dipped into the transparent gel electrolyte for 5 min and dried under an air atmosphere for 1 h 30 min. The polymer gel electrolyte coated two N-rGO fiber electrodes were sandwiched together in symmetric (N-rGO‖PVA + H_2SO_4 + aniline‖N-rGO) configurations. The electrochemical performance of the devices were examined by cyclic voltammetry (CV), galvanostatic charge–discharge (GCD), and electrochemical impedance analysis using a Bio-Logic VMP3 multi-channel potentiostat. Finally, the three fabricated devices were serially connected and integrated with CSCs in different configurations.

3. Results and discussions

3.1. Structural and morphological investigation

The XRD patterns of rGO and N-rGO (Fig. 1(a)) exhibit a broad peak around 20–30°, which indicates the reduction of GO to rGO. The calculated interlayer spacing of N-rGO was approximately 0.39 nm, which is higher than that for graphite (0.34 nm).[11] This larger interlayer spacing indicates the reduction of van der Waals forces of attraction, π–π interactions, and electrostatic interactions between the individual graphene sheets.[16] These weak interactions may be due to the reduction of conjugated carbon atoms in the basal plane of the rGO and N-rGO sheets.[16] Similarly, the XRD pattern of N-rGO further indicates that the doping of N atoms did not affect the structure of N-rGO because there were essentially no differences between the XRD patterns of rGO and N-rGO. Additionally, the absence of additional peaks in both samples reveals the phase purity of the rGO and N-rGO samples.

Raman spectroscopy was performed to analyze the presence of defects in the rGO and N-rGO samples (Fig. 1(b)). Raman spectroscopy is a non-destructive technique for the investigation of carbon-based materials. The spectra for rGO and N-rGO contain two well defined D and G bands, which are located at 1353 cm^{-1} and 1590 cm^{-1}, respectively. The D band is associated with the presence of defects in the graphene sheets and is a combination of edge and structural changes (A_{1g} symmetry mode of vibration). Similarly, the G band illustrates the emission phonon from the first-order zone midpoint and is related to sp^2 carbon vibrations in graphene domains (E_{2g} mode of the sp^2 carbon atoms).[11,16–18] The peak intensity of the D band (I_D) was higher than the intensity of the G band (I_G), which indicated the presence of defects in both samples. Generally, the degrees of defects and disorder were derived from the intensity ratio, I_D/I_G. The calculated I_D/I_G ratios were 1 and 1.091 for rGO and N-rGO, respectively. The higher I_D/I_G value for N-rGO indicated that the nitrogen atom doping increased the small sp^2 domains.[19] In other words, the increasing I_D/I_G ratio reveals the conversion of sp^3-hybridized carbons to sp^2-hybridized carbons or an increased defect density for N-rGO.[19] The shift of the D and G bands of N-rGO to higher wavenumbers indicated doping of the nitrogen atoms in the graphene sheets or bonding between N and C.[16,20] This indicated that the N atoms were successfully doped into the graphene sheets by using melamine as N source.[17]

Fig. 1(c) shows the FT-IR spectra of the rGO and N-rGO samples. The spectrum of rGO contained three different bands located at 1260 cm^{-1} (C=O), 1576 cm^{-1} (sp^2-hybridized C=C), and 1735 cm^{-1} (C=O). It also revealed the presence of some oxygen functional groups even after the hydrothermal reduction. Similarly, N-rGO also showed the same functional groups. Compared to rGO, the peak observed at 1265 cm^{-1} was broader for N-rGO. This may be due to the presence of the C–N stretching vibration at 1250 cm^{-1}. The spectrum also confirmed the doping of nitrogen atoms in the carbon sites of graphene. This result further substantiates the XRD and Raman results.

XPS was performed for the rGO and N-rGO samples to identify the different functionalities (Fig. 2). Fig. 2(a) shows the XPS survey spectra for both samples. Two prominent peaks were observed at binding energies of 284.6 and 531.94 eV, which correspond to C1s and O1s, respectively. The intensity of the C1s peak was higher than the O1s peak, which revealed the partial reduction of functional groups (*e.g.*, C=O and C–O/C–O–C). Interestingly, a small N1s peak was observed at 400 eV in N-rGO. It further confirmed that rGO was doped with N atoms. The calculated atomic amounts of C, O, and N in N-rGO were 80.36 wt%, 16.87 wt%, and 2.77 wt%, respectively. Similarly, rGO contained 83.98 wt% C and 16.02 wt% O. The deconvoluted high-resolution spectra of C1s (Fig. 2(b and c)) suggested the presence of C–C, sp^2 carbon, C=O, and π–π* shake-up features corresponding to the binding energies of 284.6, 286.02, 287.98, and 290.92 eV, respectively. Among these, the observed prominent peak at 284.6 eV confirms the presence of graphitic carbon.[21] Similarly, the deconvoluted high-resolution O1s spectra (Fig. 2(d and e)) corroborated the existence of C=O (at 531.34 eV) and C–O/C–O–C (at 533.15 eV) functional groups. The atomic percentages of the C=O and C–O/C–O–C functional groups in N-rGO were 5.56 wt% and 10.35 wt%, respectively; the atomic percentages of the same functional groups in rGO were 3.16 wt% and 10.03 wt%, respectively. N-rGO contains more active oxygen functional groups than rGO. Yang *et al.* reported a similar result for N-rGO prepared by a microwave-assisted hydrothermal method.[22] Additionally, the deconvoluted N1s spectrum (Fig. 2(f)) indicated the presence of pyrrolic N (2.28

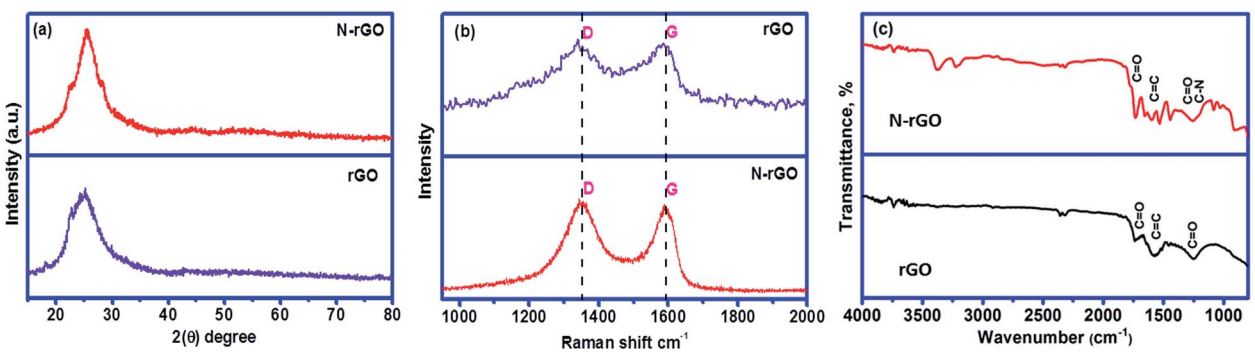

Fig. 1 (a) X-ray diffraction patterns, (b) Raman spectra, and (c) FT-IR spectra of the rGO and N-rGO samples.

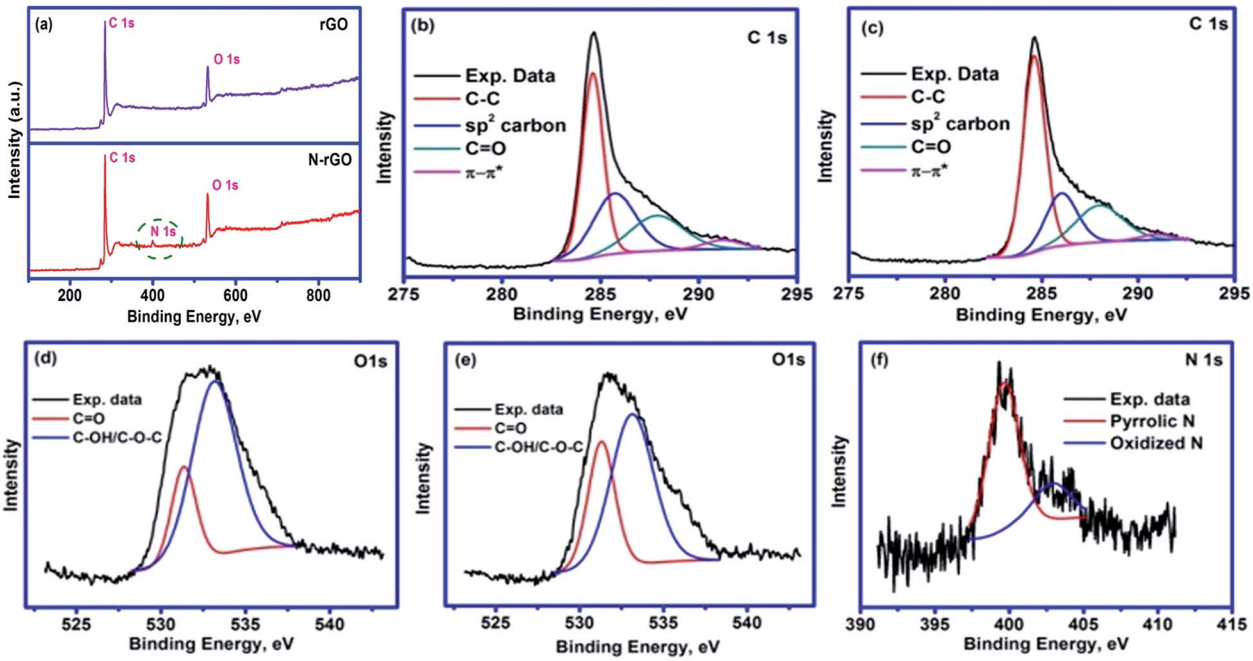

Fig. 2 (a) XPS survey spectra for rGO and N-rGO samples, (b and c) high-resolution XPS spectra of C1s in rGO and N-rGO, (d and e) high-resolution XPS spectra of O1s in rGO and N-rGO, respectively, and (f) high-resolution XPS spectrum of N1s in N-rGO.

wt%) and oxidized N (0.68 wt%) with corresponding binding energies of 399.64 and 402.92 eV, respectively. The pyrrolic nitrogen reduced the charge transfer resistance, improved the electrochemical performance, and provided a good electrochemical reversibility for the devices in aqueous electrolytes.[22–25]

The TEM images (Fig. 3(a and b)) show that the prepared N-rGO was optically transparent, which revealed that it contained few layered graphene sheets than rGO. The observed curved edges, wrinkles, and folds in the N-rGO may be due to the doping of nitrogen atoms in the carbon sites, creating defects in the sheets.[19] These wrinkles and folds on the surface of the N-rGO indicated good flexibility of the material and confirm the suitability of N-rGO for the fabrication of flexible fiber SCs. Additionally, the curved edges of the N-rGO inhibit the re-stacking of individual graphene sheets, which supports the XRD results. The inhibition of stacking favors the easy accessibility of electrolyte ions and enhances the specific capacitance

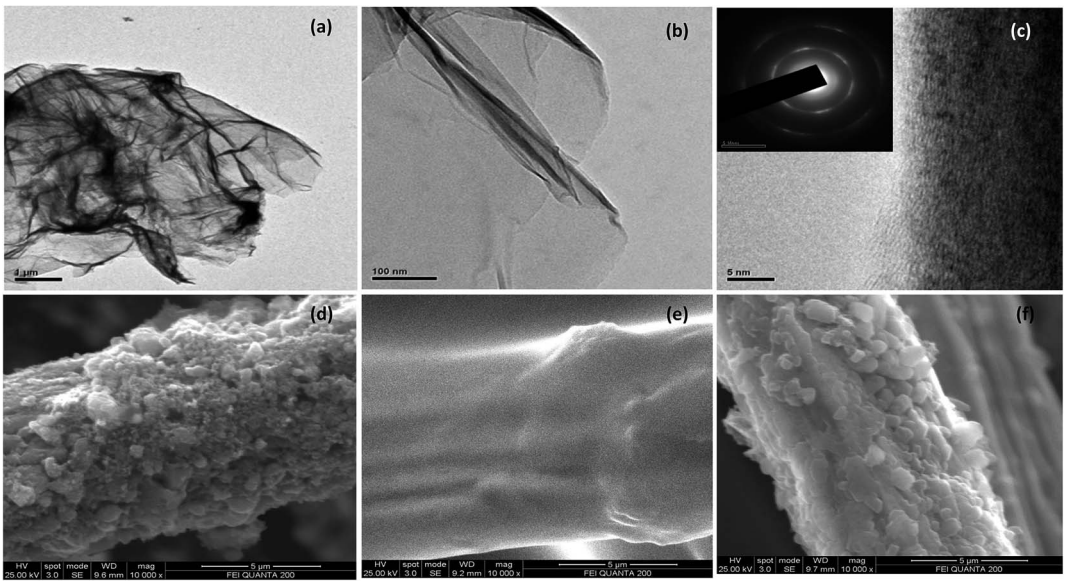

Fig. 3 (a and b) TEM and (c) HRTEM image (inset: SAED pattern) of prepared N-rGO, (d) SEM images of N-rGO coated electrode, (e) polymer electrolyte coated N-rGO electrode and (f) N-rGO electrode after 20 cycles.

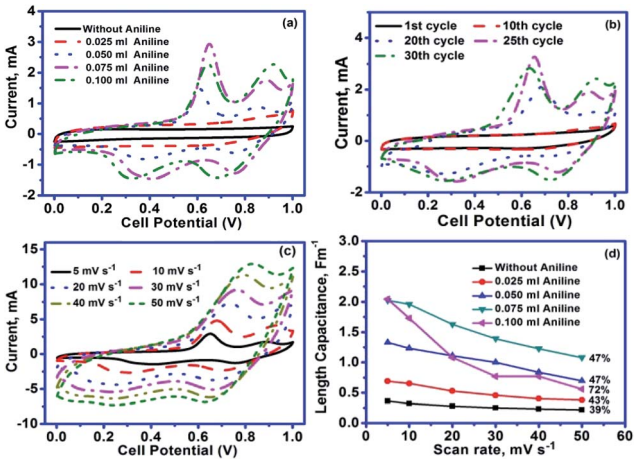

Fig. 4 Comparative (a) CV curves of the fiber rGO supercapacitor at 5 mV s^{-1}, (b and c) representative CV curves of PAH075 at different cycles and different scan rates, and (d) the scan rate dependence of length capacitance.

of the material. The HRTEM image of N-rGO (Fig. 3(c)) shows the presence of a few layered graphene sheets. There were no clear diffraction fringes due to the low crystallinity, the presence of oxygen functional groups on the graphene sheets, and the N-doping of the sample. Further, the selected area electron diffraction pattern (inset of Fig. 3(c)) shows diffraction rings with low intensity spots, indicating the non-crystalline nature of N-rGO.[26]

The SEM images envisaged the coating of N-rGO (Fig. 3(d)) on fiber substrate and polymer gel electrolyte (PVA + H_2SO_4 + aniline) coated N-rGO electrode (Fig. 3(e)). It can be seen that the N-rGO slurry was evenly coated on the surface of the fiber substrate. Similarly, Fig. 3(e) reveals that the active material was uniformly wrapped by the polymer gel electrolyte without any defects or cracks. It is believed that this uniform smooth surface of the electrode will provide good flexibility for fabricated device. In addition, this gel electrolyte coating strictly prevents the detachment of active material from fiber substrate. Fig. 3(f) shows the SEM images of the N-rGO single electrode after 20th cycles in aqueous 1 M H_2SO_4 + 0.075 mL aniline. It can be clearly seen that the formation of thin PANI layer over the fabricated electrode after cycling. It clearly evidenced that the N-rGO fiber electrode had smooth surface and also N-rGO completely wrapped with PANI. Hence, the N-rGO acts as conductive substrate and also enhances the electrochemical activity.

3.2. Electrochemical analysis of the fabricated symmetric device

The flexible fiber SC was designed by sandwiching a polymer gel electrolyte (PVA + H_2SO_4 + aniline) between two N-rGO-based electrodes.[25,27] Cyclic voltammetry was performed to determine the nature of the charge storage mechanism, to optimize the operating potential window, and to understand the effect of the aniline concentration on the electrochemical performance of flexible fiber N-rGO-based SCs. Fig. 4(a) shows the comparative CV curves (at 5 mV s^{-1}) of the symmetric device with and without the addition of aniline. A rectangular CV curve with a small broad hump was observed for the device without aniline, which indicated that the device stored the charge based on an ideal capacitive mechanism by the adsorption of electrolyte ions at the electrode/electrolyte interface and a fast surface redox reaction.[2] The presence of oxygen functional groups improved the surface wettability, electroactive surface area, and favoured the easy accessibility of electrolyte ions.[28] The partially unreduced oxygen functional groups provided additional pseudocapacitance to the material and offered a new path to oxidize aniline to polyaniline.[14,29,30] The atomic percentage of N1s may be more favorable for enhancing the electrochemical performance of the material. Recently, Li *et al.* reported that the optimum atomic weight percentage of N1s was 2.97 wt%; above this value, the specific capacitance, rate capability, and coulombic efficiency deteriorated.[31] The observed redox properties originated from the unreduced oxygen functional groups (eqn (1)–(3)) and the available N-heteroatoms (eqn (4)).[10,32,33]

$$>C\text{–}OH \leftrightarrow >C{=}O + H^+ + e^- \quad (1)$$

$$\text{–}COOH \leftrightarrow \text{–}COO^- + H^+ + e^- \quad (2)$$

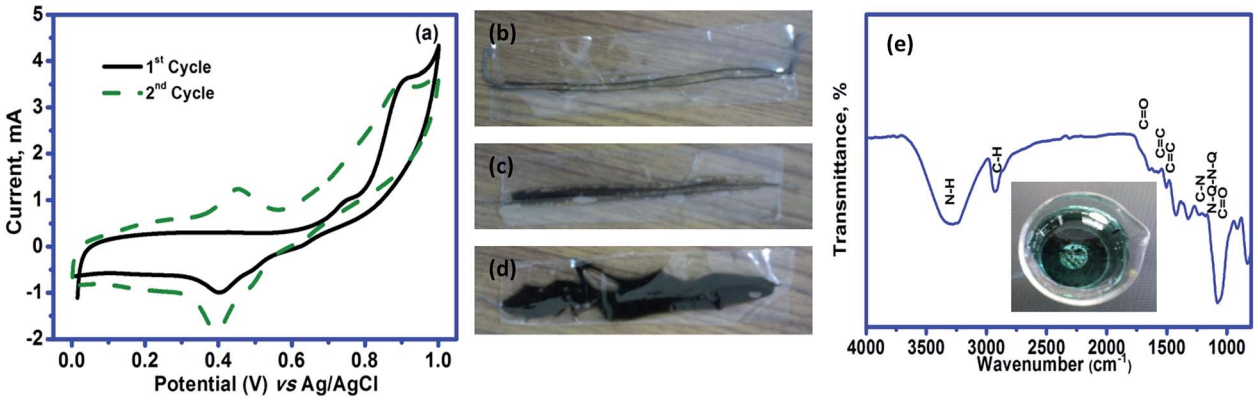

Fig. 5 (a) CV curves of N-rGO electrode at 5 mV s^{-1}, photographic images of the fabricated device after (b) 10th, (c) 20th, and (d) 30th cycles, and (e) FT-IR spectrum of the N-rGO after 25th cycle (inset: photograph of the scratched material dispersed in distilled water).

$$>C{=}O + e^- \leftrightarrow >C{-}O^- \quad (3)$$

$$-CH{-}NH_2 + H_2O \leftrightarrow -CH{-}NHOH + 2e^- + 2H^+ \quad (4)$$

The presence of oxygen functional groups and N atoms provided a supplementary pseudocapacitance to the device. Furthermore, a pair of oxidation and reduction waves was realized by adding aniline as a redox additive. The peak currents and area under the CV curves increased with the concentration of aniline from 0.025 mL to 0.1 mL, which indicated improved charge storage for the devices. The amount of charge stored in the device is given by the area under the CV curve. The flexible fiber N-rGO SC covers more current area in PAH025, PAH050, PAH075, and PAH100 than PAH000 because of the conversion of aniline to polyaniline.

To identify the activity of the aniline redox additive in the electrolyte, a CV cycling stability test was performed. The representative CV curves for the N-rGO device prepared using 0.075 mL of aniline are shown in Fig. 4(b) at various cycles. No significant current increase was observed due to the redox properties during the initial 10 cycles. This confirmed that the flexible fiber SC stored the maximum amount of charge by double layer capacitance rather than pseudocapacitance up to 10 cycles. After 10 cycles, an outstanding pair of redox waves clearly indicated that the aniline monomers were adsorbed on the surface of the electrodes and were completely converted to polyaniline. The oxidation potential of aniline was lower than the first cycle, due to the self-catalytic effect of polyaniline (PANI).[34]

In Fig. 4(b), the first oxidation wave at 0.65 V (25th cycle) suggested the conversion of the fully reduced state of leucoemeraldine to the half-oxidized polaronicemeraldine salt form of PANI. In contrast, the oxidation peak recorded at 0.88 V implied the transition of the half-oxidized emeraldine state to the fully oxidized dipolaronic pernigraniline state. The corresponding reduction waves were observed at 0.75 V and 0.31 V. This confirms the good electrochemical reversibility of PANI during the charge–discharge process. Here, the N atoms were present in the amines of leucoemeraldine and in the imines of pernigraniline. The amine to imine ratio was approximately 1 for emeraldine.[34] The absence of any additional peaks between the above-mentioned peaks indicated that there was no degradation of PANI.[35]

Fig. 4(c) explains the effect of the scan rate on the CV curves for the optimized PAH075. The peak current values increased with increasing scan rates because the peak current is directly proportional to the scan rate. Similarly, the oxidation peak shifted towards a higher positive potential, and the reduction peaks drifted toward a lower potential. At a higher scan rate, the peaks broadened due to the electrode resistance. A pair of redox peaks occurred even at a higher scan rate of 50 mV s^{-1}, suggesting the fast electron transfer from PANI to the current collector *via* N-rGO. Irrespective of the scan rate, the two pair of redox regions with potential independent current regions validated the co-existence of pseudocapacitive and electric double-layer (EDL) capacitive properties.[10] Similar observations were noted for the other electrodes (Fig. S2(b–d)†). However, at high aniline concentrations (PAH100), these peaks disappeared and a new peak emerged that indicated the degradation of PANI into soluble and insoluble products at a high scan rate (such as benzoquinone, quinoemine end-groups, and *ortho*-coupled polymers).[35] In addition, the redox peaks were largely broadened compared to PAH025, PAH050, and PAH075 because of the high electrode resistance. This led to a drastic loss of the specific capacitance in PAH100. The length specific capacitance of the device was calculated from the CV results using the following equation:

$$C_l = \frac{\int i\mathrm{d}t}{l \times V \times \nu} \ \mathrm{F\ cm^{-1}} \quad (5)$$

here, $\int i\mathrm{d}t$ refers to the current area under the CV curve, l is total length of the device (cm), V is the potential window of the device (V), and ν is the scan rate (mV s^{-1}). Fig. 4(d) compares the effect of the scan rate on the length capacitance of the devices. The calculated length capacitances of the device were 0.36, 0.77, 1.33, 2.02, and 2.05 F m^{-1} in PAH000, PAH025, PAH050, PAH075, and PAH100 electrolytes, respectively. This demonstrates that the length capacitance increased with respect to the aniline concentrations. The length capacitance improved by 5.7-fold, when aniline was used as a redox additive. This improved

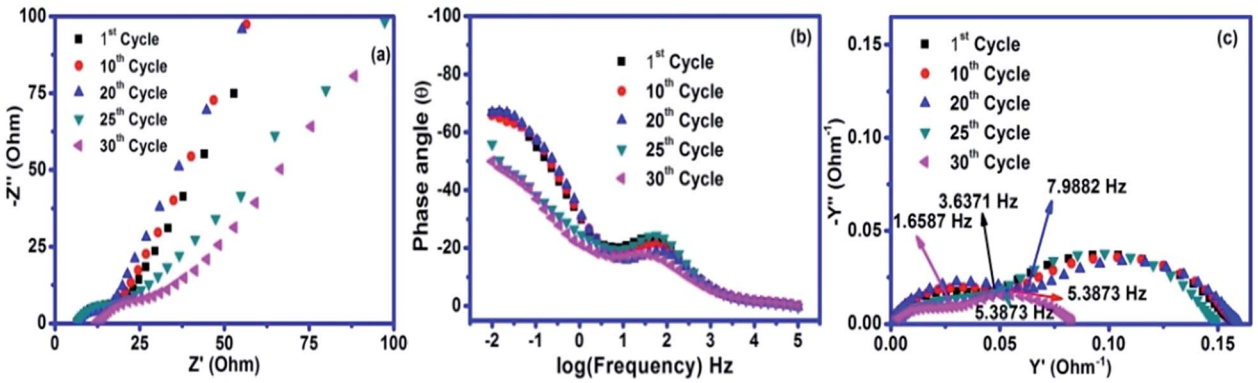

Fig. 6 (a) Nyquist, (b) Bode, and (c) admittance plots of the N-rGO fiber supercapacitor (PAH075) at various cycles.

length capacitance may be ascribed to the fast faradaic reaction of polyaniline. Similarly, the hydrophilic property of polyaniline also improved the wettability of the electrode and supported the fast accessibility of the electrolyte ions into the electrode.[36] However, the loss of the length capacitance was considerable at high aniline concentrations due to the increase of the electrode resistance, irreversibility of the redox reactions, and increased degradation of PANI. The length capacitance losses were 39%, 43%, 47%, 47%, and 72% for PAH000, PAH025, PAH050, PAH075, and PAH100, respectively. A small length capacitance loss implied a good rate capability for the device. In all cases, the devices delivered a high length capacitance at a low scan rate that decreased when the scan rate increased. The shorter time for electrolyte ion use with the active electrode material led to a reduced length capacitance.[37]

To validate the self-catalytic effect, electrochemical analysis was performed in a three-electrode system in the presence of aniline as a redox additive (Fig. 5(a)). The first oxidation peak was at 0.75 V *vs.* Ag/AgCl during the 1st cycle, which shifted to a lower oxidation potential of 0.45 V *vs.* Ag/AgCl for the 2nd cycle. This was due to the self-catalytic effect of PANI. Subsequently, the peak current increased with successive cycles.[34,38] These results further suggested the co-existence of pseudocapacitive and double-layer capacitive mechanisms. After 25 cycles, the peak current diminished, which indicated the irreversibility of the PANI electrochemical reaction and complete conversion of PANI.[34] The conversion of the aniline monomer to polyaniline was explained elsewhere.[34–36] During the electrochemical oxidation, the aniline in the polymer electrolyte was adsorbed on the surface of the N-rGO electrode through the electrostatic interaction between the negatively charged unreduced oxygen functional groups of N-rGO and the positively charged amino group of aniline. Initially, the aniline monomer was converted into cation radicals by releasing an electron. Then, the lone electron in the cation radical was delocalized into the *para*-position. Subsequently, it reacted with another cation radical to produce the head to tail addition. The lone electron delocalized cation radicals reacted with aniline to produce intermediate products that reacted with another aniline molecule to produce polyaniline. This process continued until the oxidation of aniline was complete.[35,36]

The photographs in Fig. 5(b–e) support the above postulates. The light green color on the surface of the electrode (Fig. 5(b)) indicated the polymerization of aniline starts at the 10th cycle. Subsequently, after the 20th cycle (Fig. 5(c)), the green color was clearly visible on the surface of the electrode. It indicated that the concentration of polyaniline increased in the subsequent cycles. After the 30th cycle (Fig. 5(d)), the entire surface of the electrode was green, which provided evidence for the complete formation of polyaniline. Surprisingly, there were no short circuits during the electrochemical reaction due to the insulating property of polyvinyl alcohol. To validate the above observations, the green material was scratched off the fiber electrode and dispersed in doubly distilled water. The dispersed solution appeared as green colour (inset: Fig. 5(e)), which supports the formation of PANI. This supports the formation of polyaniline.

FT-IR analysis was performed after the 30th cycle (Fig. 5(e)). It showed the presence of the characteristic peaks of PANI in addition to the oxygen functional groups of N-rGO. The C=C stretching modes of the benzenoid and quinoid rings of PANI were observed at 1514 and 1573 cm^{-1}, respectively. Further, the

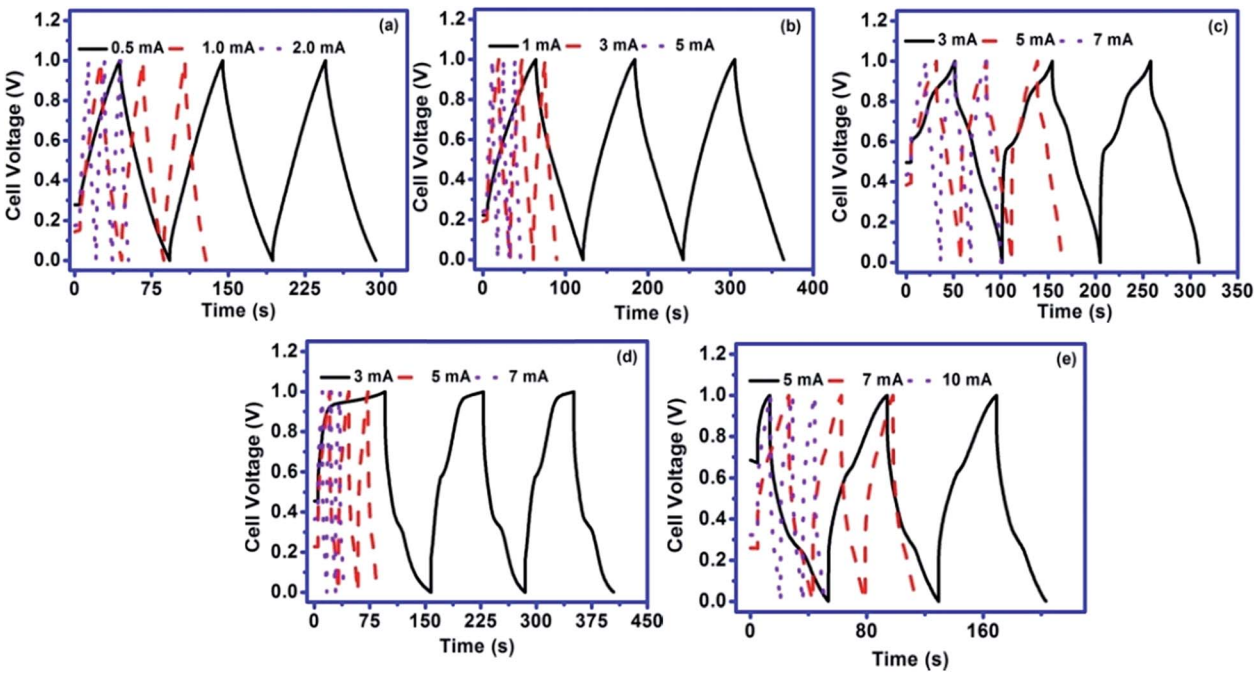

Fig. 7 GCD curves of the N-rGO fiber supercapacitor at different currents in (a) PAH000, (b) PAH025, (c) PAH050, (d) PAH075, and (e) PAH100 gel electrolytes.

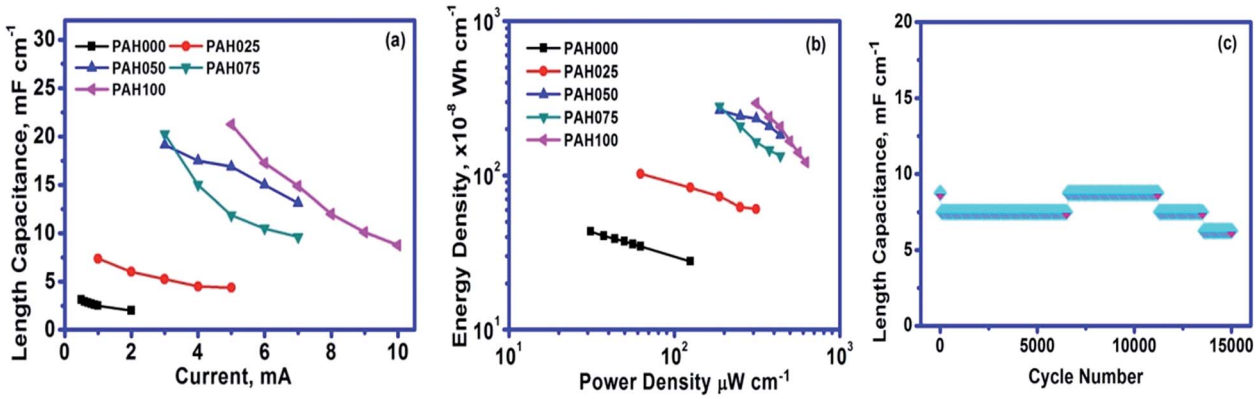

Fig. 8 (a) Variation of length capacitance with applied current, (b) change in energy density with power density, and (c) representative cycle life of rGO fiber supercapacitor in PAH075 over 15 000 cycles.

overlapped N-Q–N-Q stretching band at 1134 cm^{-1} indicated the existence of covalent bonding between N-rGO and PANI and revealed the conversion of the aniline redox additive to PANI during the electrochemical cycling. Additionally, a C–H bending vibration was observed at 2936 cm^{-1}. Surprisingly, a broad band was observed around 3250 cm^{-1}, which is related to the stretching vibration of N–H and O–H bonds. These modes were not observed for the pristine rGO and N-rGO electrodes. The presence of N–H bonds supports the fast charge transfer between N-rGO and PANI.[29,39–43]

Electrochemical impedance spectroscopy was performed (frequency range: 0.10 MHz to 10 mHz, perturbation potential: 10 mV) to understand the charge transfer kinetics at the electrode/electrolyte interface, the internal resistance, the diffusive resistance, and the capacitive behavior of the device. The device behaved as a resistor in the high-frequency regions and as a capacitor in the low-frequency regions. In general, the Nyquist plot consisted of three different regions. The high frequency region describes the equivalent serial resistance (R_{ESR}) of the device. R_{ESR} is the combination of the interfacial resistance at the current collector and the active material, the intrinsic resistance of the active material, and the solution resistance. A small semicircle was observed in the mid-frequency region. The diameter of the semicircle indicated the charge transfer resistance at the electrode/electrolyte interface (R_{CT}). Similarly, the low-frequency region, a tail, clarified the capacitance of the device. If the tail had a phase angle of 90° from the real axis, then the device had an ideal capacitive behavior and a low diffusive resistance. When the tail had a phase angle of 45° from the real axis, the device had a highly diffusive resistance and pseudocapacitive properties. A phase angle from 45° to 90° indicated the coexistence of both properties.[10,11,18] The Nyquist plot (Fig. 6(a)) shows that the intersection of a semicircle in the high-frequency region on the real axis of impedance (or R_{ESR}) is almost the same up to the 25th cycle (*i.e.*, 6.64, 6.54, 6.46, and 6.94 Ω for the 1st, 10th, 20th, and 25th cycles, respectively). The R_{ESR} value drastically increased and reached 12.68 Ω at the 30th cycle, which led to a decrease of the device capacitance. In contrast, the charge transfer resistance decreased up to the 20th cycle, such as 7.86, 6.51, and 5.28 Ω for 1st, 10th and 20th cycle respectively. A smaller R_{CT} value indicated a fast charge transfer rate due to the good electrical contact between N-rGO and the substrate. After that, the charge transfer resistance increased to 9.027 Ω and 10.87 Ω for the 25th and 30th cycles, respectively. A higher R_{CT} value indicated a slow charge transfer rate, which may be due to an increase of the PANI thickness on the surface of the electrode material. In other words, it may be due to the low percolation threshold because only the top layer can provide the capacitance.[44] In contrast, the tail was shifted toward the real axis of impedance with

Table 1 Summary of the comparative electrochemical performance of N-rGO with previous reports

Material	Length capacitance	Current density/scan rate	Electrolyte	References
rGO	27 mF cm^{-1}	2 μA	PVA/H_2SO_4	46
Multi-walled carbon nanotube/ordered mesoporous carbon	1.91 mF cm^{-1}	10 μA	PVA/H_3PO_4	47
Carbon nanotube	29 μF cm^{-1}	1 × 10^{-7} A	PVA/H_3PO_4	48
Ink pen-based active electrode	0.504 mF cm^{-1}	0.083 mA cm^{-2}	PVA/H_2SO_4	49
Activated carbon	0.1 mF cm^{-1}	40 μA	PVA/H_3PO_4	50
rGO/CNT	5.3 mF cm^{-1}	0.1 mA cm^{-2}	PVA/H_3PO_4	51
Carbon microfiber bundles coated with MWCNT	6.3 mF cm^{-1}	2 mV s^{-1}	PVA/H_3PO_4	52
Ni_3S_2||pen ink	8.16 mF cm^{-1}	0.2 A g^{-1}	PVA/KOH	53
PPy/MnO_2/rGO	15.5 mF cm^{-1}	11 mA cm^{-3}	PVA/H_3PO_4	54
N-rGO	21.25 mF cm^{-1}	5 mA	PVA + H_2SO_4 + aniline	Present work

Table 2 Summary of the comparative cyclic stability of N-rGO with previous reports

Device	Capacitance retention (%)	Cycles	References
PANI/graphene|PVA + H_3PO_4|PANI/graphene	89	1000	56
Functionalized graphene|6 M KOH|functionalized graphene	88	10 000	57
CNT@PANI|PVA + H_2SO_4|CNT@PANI	91	800	58
PANI|1 M H_2SO_4|PANI	78	1000	59
PANI/CSA|0.5 M H_2SO_4|PANI/CSA	88	500	60
G-PNF|H_2SO_4|G-PNF	79	800	61
PANI|H_2SO_4|PANI	73	2000	62
PANI/graphene/PANI|H_2SO_4|PANI/graphene/PANI	84	1000	63
PANI|PVA + H_2SO_4|PANI	86	1000	64
GH-PANI/GP|PVA + 1 M H_2SO_4|GH-PANI/GP	85.6	5000	65
rGO-F/PANI|H_2SO_4|rGO-F/PANI	80	5000	66
N-rGO|PVA + H_2SO_4 + aniline|N-rGO	72	15 000	Present work

increasing cycles, which indicated an increase of the pseudocapacitive property of the device in the low-frequency region. These results revealed that after the 25th cycle, the equivalent serial and charge transfer resistance values largely increased and the tail shifted toward the real axis (this supports the CV results). Fig. 6(b) shows the Bode plot of the device. The phase angle decreased with cycling, which indicated an increase of the pseudocapacitive nature of the device, in agreement with the CV curve. Additionally, the broad peak in the high-frequency region corresponded to the diffusive resistance of the device. The peak shifted toward the high-frequency region up to the 20th cycle, which revealed a decrease of the diffusive resistance of the device. The reduction of the diffusive resistance of the ions into the device improved the electrochemical accessibility of electrolyte ions and the capacitance of the device.[11] Then, the peak shifted to a lower frequency, which was due to the increased diffusive resistance of the device and reduced the capacitance of the device.[11,18] The knee frequency (calculated from the admittance plot Fig. 6(c)) increased with an increasing number of cycles (up to the 20th cycle) followed by a small shift toward the lower frequency region. The knee frequencies were 3.63, 5.38, 7.98, 5.38, and 1.65 Hz. In contrast, the relaxation time decreased up to the 20th cycle and then increased. The relaxation time corresponded to the device change from resistive behavior to capacitive behavior. The calculated relaxation times were 274, 185, 125, 185, and 602 ms for the 1st, 10th, 20th, 25th, and 30th cycles, respectively. Overall, the initial cycles were crucial to enhance the electrochemical performance of the device, which significantly enhanced the capacitance behavior by increasing the pseudocapacitive contribution from the redox additive, changing the charge transfer, diffusive, and equivalent serial resistances, and inducing the conversion of aniline to PANI.

The GCD analysis was performed without aniline and with various concentrations of aniline to further validate the CV results. Fig. 7(a–e) shows the GCD curve of devices at different currents. Fig. 7(a) shows linear charge and discharge behaviors, with a maximum contribution from the EDLC capacitance rather than Faradic capacitance. The short discharge time was due to the dominant ideal capacitive charge storage mechanism. However, when aniline was used as the redox additive (Fig. 7(b–e)), the charge/discharge curves were nonlinear and two redox plateau regions were observed, which demonstrated the faradaic charge storage mechanism of PANI. The discharge time increased due to the combination of diffusion-controlled charge storage mechanisms.[34] The GCD curve supported the data from the CV curves, which demonstrated the coexistence of both EDL capacitive and pseudocapacitive properties.[45] The operating current of the device was remarkably improved in the presence of aniline as a redox additive. Hence, aniline played a dual role of increasing both the capacitance and the current of the device. The length capacitance values were calculated from the discharge curve at different currents and the values are shown in Fig. 8(a). The length capacitance of the device was found to be higher in the presence of aniline than in its absence. The maximum length capacitance of 21.25 mF cm^{-1} was delivered by the device at a current of 5 mA in the PAH100 electrolyte (this value was predicted from the discharge curve). However, at higher aniline concentrations, the length capacitance loss was massive with currents. PAH075 was determined as the optimum electrolyte for the device based on its excellent electrochemical performance, low electrode resistance, lesser capacitance loss, and fast charge transport from PANI to the

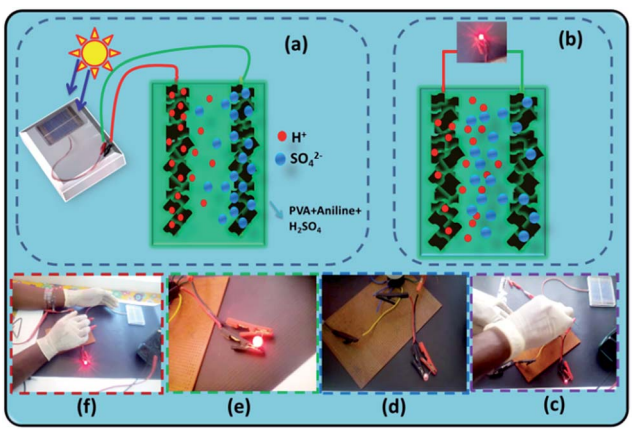

Fig. 9 (a and b) Schematic representation of charging and discharging mode of device and (c–f) glowing of an LED with different configurations.

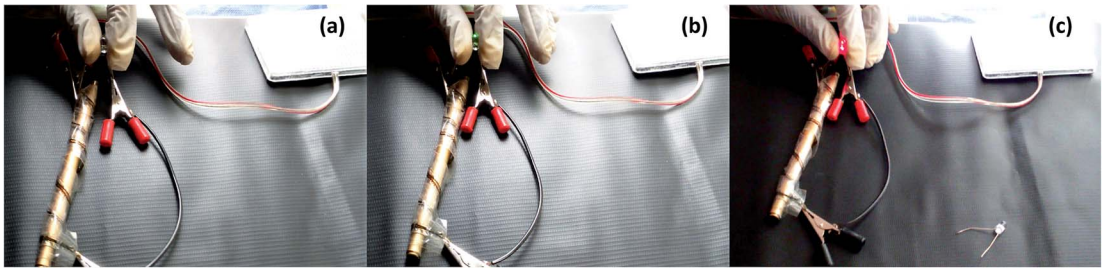

Fig. 10 The (a) charging mode of device with CSC and (b and c) powering of green & red LEDs.

current collector *via* N-rGO. The length capacitance was higher than or comparable to previous reports which was given in Table 1.[55] The energy and power density are two essential parameters for evaluating the electrochemical performance of a device. From the Ragone plot (Fig. 8(b)), one can see that the device delivered a high energy density with aniline as a redox additive. The maximum delivered energy density of the fabricated device was 295×10^{-8} W h cm^{-1} at a power density of 312 μW cm^{-1}. To demonstrate the suitability of the device for a long life, the cycling stability of one representative device (PAH075) was carried over 15 000 cycles at a current of 7 mA (Fig. 8(c)). The length capacitance decreased initially and maintained 86% of its initial capacity until the next 6500 cycles. This may be due to the low wettability of the electrode materials during the initial charge–discharge. Surprisingly, the length capacitance of the device increased to its initial value and was maintained for up to 11 200 cycles. After 11 200 cycles, the length capacitance value decreased gradually to 72% capacity retention. The reason for the loss of the length capacitance at higher charge discharge cycles was attributed to the presence of PANI. PANI underwent a volume expansion and contraction during the charging–discharging cycles. However, the capacitance retention was comparably higher than that previously reported for functionalized graphene and PANI-related devices (Table 2). From the above analysis, PAH075 was found to be an excellent polymer gel electrolyte for N-rGO flexible fiber SCs based on the electrochemical performances, *e.g.*, capacitance, capacitance retention, energy density, and cyclic stability.

3.3. Real time applications

Despite its excellent electrochemical performances, the device must be tested for practical applications. To address the suitability of the device in real time applications, three flexible fiber N-rGO SCs were serially connected to power light emitting diodes (LEDs). To meet the wider demand of N-rGO SCs, the devices were charged in different flexible modes, *e.g.*, normal, spiral, zigzag, and ring using a CSC. Each electrode was 6 cm long with a 1 V potential window. Fig. 9(a) shows the schematic representation of charge storage mechanism of N-rGO by CSC. During charge, the H^+ and SO_4^{2-} ions from electrolyte were approached to the oppositely charged electrodes and adsorbed on the surface of the electrode.

Additionally, the PANI was undergone oxidation reaction. Subsequently, the stored charge was used to glow the red LED. In this situation, the ions from electrode are back to diffusive layer and PANI gets reduced (Fig. 9(b)). The device was charged (video given in ESI†) up to 2.2 V using a CSC for a few seconds and was able to power the LED for a few minutes. Fig. 9(c–f) represents the discharging modes of the device in different flexible configurations. Even in flexible modes, the device powered the red LED. This demonstrates the excellent power-delivery capability of the device during the flexible configurations, *e.g.*, spiral, zigzag, and ring-type. It illustrates that the fabricated device is reliable for integration with various energy conversion devices and will be useful for energy storage in flexible displays, bendable mobile phones, and other electronic goods.

In order to identify the durability and potential of driving different coloured LEDs (for different voltage), the fabricated spiral supercapacitors (10 months older), is charged with the help of CSC. Interestingly, the device was charged within few seconds (Fig. 10(a)), and it could power both green and red LEDs for minutes (refer attached videos†). It indicates that the good power deliverable capability of the device. Even after fabricating 10 months later, the device has power greatly both green and red LEDs (Fig. 10(b and c)).

4. Conclusions

The fabricated flexible fiber rGO devices showed an excellent electrochemical performance. The pyrrolic N provided additional pseudocapacitance and improved the wettability of the material. Similarly, the presence of the partially unreduced oxygen functional groups enhanced the pseudocapacitance and converted the aniline to polyaniline during the electrochemical reaction. Surprisingly, the capacitance and energy density improved using aniline as a redox additive in the PVA + H_2SO_4 gel electrolyte. The conversion of aniline to polyaniline contributed additional pseudocapacitance to the N-rGO during cycling. At higher aniline concentrations, the length capacitance loss was higher than for lower concentrations of aniline (which may be due to the low percolation threshold). In addition, the flexible fiber N-rGO devices showed an excellent capacitance retention over 15 000 cycles. Thus, the polymer gel electrolyte adds safety and flexibility to the device in the process of fabrication. The N-rGO device can be integrated with CSCs, which illustrates the reliability of the device to combine with other energy conversion devices. Finally, the excellent power

delivery of the device in different flexible configurations confirms the suitability of the device for flexible/wearable applications.

Acknowledgements

The authors would like to thank the Department of Science and Technology (DST-SERB) and the Government of India for providing financial support (SR/FTP/PS-80/2009) under the "Fast Track Young Scientist" scheme.

References

1 Y. Shao, M. F. El-Kady, L. J. Wang, Q. Zhang, Y. Li, H. Wang, M. F. Mousavi and R. B. Kaner, *Chem. Soc. Rev.*, 2015, **44**, 3639–3665.
2 B. Liu, B. Liu, X. Wang, D. Chen, Z. Fan and G. Shen, *Nano Energy*, 2014, **10**, 99–107.
3 H. Gao, F. Xiao, C. B. Ching and H. Duan, *ACS Appl. Mater. Interfaces*, 2012, **4**, 7020–7026.
4 J. Bae, M. K. Song, Y. J. Park, J. M. Kim, M. Liu and Z. L. Wang, *Angew. Chem., Int. Ed.*, 2011, **50**, 1683–1687.
5 K. Naoi, S. Ishimoto, J. Miyamoto and W. Naoi, *Energy Environ. Sci.*, 2012, **5**, 9363–9373.
6 M. Zhi, C. Xiang, J. Li, M. Li and N. Wu, *Nanoscale*, 2013, **5**, 72–88.
7 L. L. Zhang and X. S. Zhao, *Chem. Soc. Rev.*, 2009, **38**, 2520–2531.
8 S. Kim, G. Park, P. Sennu, S. Lee, K. Choi, J. Oh, Y.-S. Lee and S. Park, *RSC Adv.*, 2015, **5**, 86237–86241.
9 S. Park and R. S. Ruoff, *Curr. Opin. Colloid Interface Sci.*, 2015, **20**, 322–328.
10 S. T. Senthilkumar, K. V. Sankar, J. S. Melo, A. Gedanken and R. K. Selvan, *Carbon and its hybrid composites as advanced electrode materials for supercapacitors*, WILEY-Scrivener Publishing LLC, USA, 2014, pp. 399–432.
11 K. V. Sankar and R. K. Selvan, *Carbon*, 2015, **90**, 260–273.
12 K. V. Sankar and R. K. Selvan, *J. Power Sources*, 2015, **275**, 399–407.
13 X. Wang, G. Sun, P. Routh, D.-H. Kim, W. Huang and P. Chen, *Chem. Soc. Rev.*, 2014, **43**, 7067–7098.
14 G. Xin, Y. Wang, X. Liu, J. Zhang, Y. Wang, J. Huang and Y. Zang, *Electrochim. Acta*, 2015, **167**, 254–261.
15 X. Fan, C. Yu, J. Yang, Z. Ling and J. Qiu, *Carbon*, 2014, **70**, 130–141.
16 G. Luo, L. Liu, J. Zhang, G. Li, B. Wang and J. Zhao, *ACS Appl. Mater. Interfaces*, 2013, **5**, 11184–11193.
17 T.-T. Lin, W.-H. Lai, Q.-F. Lü and Y. Yu, *Electrochim. Acta*, 2015, **178**, 517–524.
18 N. Chen, X. Huang and L. Qu, *Phys. Chem. Chem. Phys.*, 2015, **17**, 32077–32098.
19 K. V. Sankar and R. K. Selvan, *RSC Adv.*, 2014, **4**, 17555–17566.
20 H. Zhang, T. Kuila, N. H. Kim, D. S. Yu and J. H. Lee, *Carbon*, 2014, **69**, 66–78.
21 H. Cao, X. Zhou, Z. Qin and Z. Liu, *Carbon*, 2013, **56**, 218–223.
22 J. Yang, M. R. Jo, M. Kang, Y. S. Huh, H. Jung and Y.-M. Kang, *Carbon*, 2014, **73**, 106–113.
23 K. Fujisawa, R. Cruz-Silva, K.-S. Yang, Y. A. Kim, T. Hayashi, M. Endo, M. Terrones and M. S. Dresselhaus, *J. Mater. Chem. A*, 2014, **2**, 9532–9540.
24 F. M. Hassan, V. Chabot, J. Li, B. K. Kim, L. Ricardez-Sandoval and A. Yu, *J. Mater. Chem. A*, 2013, **1**, 2904–2912.
25 S. Yang, X. Song, P. Zhang and L. Gao, *J. Mater. Chem. A*, 2013, **1**, 14162–14169.
26 Y. Lu, F. Zhang, T. Zhang, K. Leng, L. Zhang, X. Yang, Y. Ma, Y. Huang, M. Zhang and Y. Chen, *Carbon*, 2013, **63**, 508–516.
27 Y. Yan, T. Kuila, N. H. Kim and J. H. Lee, *Carbon*, 2014, **74**, 195–206.
28 G. Park, S. K. Park, J. Han, T. Y. Ko, S. Lee, J. Oh, S. Ryu, H. S. Park and S. Park, *RSC Adv.*, 2014, **4**, 36377–36384.
29 M. Kim, C. Lee, Y. D. Seo, S. Cho, J. Kim, G. Lee, Y. K. Kim and J. Jang, *Chem. Mater.*, 2015, **27**, 6238–6248.
30 Z. Lin, G. Waller, Y. Liu, M. Liu and C.-P. Wong, *Adv. Energy Mater.*, 2012, **2**, 884–888.
31 B. Li, F. Dai, Q. Xiao, L. Yang, J. Shen, C. Zhang and M. Cai, *Energy Environ. Sci.*, 2016, **9**, 102–106.
32 D. Yu, K. Goh, H. Wang, L. Wei, W. Jiang, Q. Zhang, L. Dai and Y. Chen, *Nat. Nanotechnol.*, 2014, **9**, 555–562.
33 L. Sun, L. Wang, C. Tian, T. Tan, Y. Xie, K. Shi, M. Li and H. Fu, *RSC Adv.*, 2012, **2**, 4498–4506.
34 X.-M. Feng, R.-M. Li, Y.-W. Ma, R.-F. Chen, N.-E. Shi, Q.-L. Fan and W. Huang, *Adv. Funct. Mater.*, 2011, **21**, 2989–2996.
35 B. Jugovic, M. Gvozdenovic, J. Stevanovic, T. Trisovic and B. Grgur, *Mater. Chem. Phys.*, 2009, **114**, 939–942.
36 H.-P. Cong, X.-C. Ren, P. Wang and S.-H. Yu, *Energy Environ. Sci.*, 2013, **6**, 1185–1191.
37 K. V. Sankar, D. Kalpana and R. K. Selvan, *J. Appl. Electrochem.*, 2012, **42**, 463–470.
38 S. K. Mondal, K. Barai and N. Munichandraiah, *Electrochim. Acta*, 2007, **52**, 3258–3264.
39 V. Georgakilas, M. Otyepka, A. B. Bourlinos, V. Chandra, N. Kim, K. Christian Kemp, P. Hobza, R. Zboril and K. S. Kim, *Chem. Rev.*, 2012, **112**, 6156–6214.
40 M. Kotal, A. K. Thakur and A. K. Bhowmick, *ACS Appl. Mater. Interfaces*, 2013, **5**, 8374–8376.
41 L. Wang, Y. Ye, X. Lu, Z. Wen, Z. Li, H. Hou and Y. Song, *Sci. Rep.*, 2013, **3**, 3568–3577.
42 X.-Y. Peng, F. Luan, X.-X. Liu, D. Diamond and K.-T. Lau, *Electrochim. Acta*, 2009, **54**, 6172–6177.
43 L. Wang, X. Feng, L. Ren, Q. Piao, J. Zhong, Y. Wang, H. Li, Y. Chen and B. Wang, *J. Am. Chem. Soc.*, 2015, **137**, 4920–4923.
44 L. Lai, H. Yang, L. Wang, B. K. Teh, J. Zhong, H. Chou, L. Chen, W. Chen, Z. Shen, R. S. Ruoff and J. Lin, *ACS Nano*, 2012, **6**, 5941–5951.
45 J. Ren, L. Li, C. Chen, X. Chen, Z. Cai, L. Qiu, Y. Wang, X. Zhu and H. Peng, *Adv. Mater.*, 2013, **25**, 1155–1159.
46 Y. Meng, Y. Zhao, C. Hu, H. Cheng, Y. Hu, Z. Zhang, G. Shi and L. Qu, *Adv. Mater.*, 2013, **25**, 2326–2331.
47 J. Ren, W. Bai, G. Guan, Y. Zhang and H. Peng, *Adv. Mater.*, 2013, **25**, 5965–5970.

48 X. Chen, L. Qiu, J. Ren, G. Guan, H. Lin, Z. Zhang, P. Chen, Y. Wang and H. Peng, *Adv. Mater.*, 2013, **25**, 6436–6441.
49 Y. Fu, X. Cai, H. Wu, Z. Lv, S. Hou, M. Peng, X. Yu and D. Zou, *Adv. Mater.*, 2012, **24**, 5713–5718.
50 D. Harrison, F. Qiu, J. Fyson, Y. Xu, P. Evans and D. Southee, *Phys. Chem. Chem. Phys.*, 2013, **15**, 12215–12219.
51 L. Kou, T. Huang, B. Zheng, Y. Han, X. Zhao, K. Gopalasamy, H. Sun and C. Gao, *Nat. Commun.*, 2014, **5**, 3754–3764.
52 J. Wen, S. Li, K. Zhou, Z. Song, B. Li, Z. Chen, T. Chen, Y. Guo and G. Fang, *J. Power Sources*, 2016, **324**, 325–333.
53 Y. Huang, H. Hu, Y. Huang, M. Zhu, W. Meng, C. Liu, Z. Pei, C. Hao, Z. Wang and C. Zhi, *ACS Nano*, 2015, **9**, 4766–4775.
54 L. Dong, C. Xu, Y. Li, Z.-H. Huang, F. Kang, Q.-H. Yang and X. Zhao, *J. Mater. Chem. A*, 2016, **4**, 4659–4685.
55 V. T. Le, H. Kim, A. Ghosh, J. Kim, J. Chang, Q. A. Vu, D. T. Pham, J. Lee, S.-W. Kim and Y. H. Lee, *ACS Nano*, 2013, **7**, 5940–5947.
56 Y. Xie, Y. Liu, Y. Zhao, Y. H. Tsang, S. P. Lau, H. Huang and Y. Chai, *J. Mater. Chem. A*, 2014, **2**, 9142–9149.
57 Y. Fang, B. Luo, Y. Jia, X. Li, B. Wang, Q. Song and F. Kang, *Adv. Mater.*, 2012, **24**, 6348–6355.
58 K. Wang, Q. Meng, Y. Zhang, Z. Wei and M. Miao, *Adv. Mater.*, 2013, **25**, 1494–1498.
59 U. Male, B. S. Singu and P. Srinivasan, *J. Appl. Polym. Sci.*, 2015, **132**, 42013–42021.
60 S. Cho, K.-H. Shin and J. Jang, *ACS Appl. Mater. Interfaces*, 2013, **5**, 9186–9193.
61 Q. Wu, Y. Xu, Z. Yao, A. Liu and G. Shi, *ACS Nano*, 2010, **4**, 1963–1970.
62 B. Rajender and S. Palaniappan, *New J. Chem.*, 2015, **39**, 5382–5388.
63 Z. Tong, Y. Yang, J. Wang, J. Zhao, B.-L. Su and Y. Li, *J. Mater. Chem. A*, 2014, **2**, 4642–4651.
64 K. Wang, X. Zhang, C. Li, H. Zhang, X. Sun, N. Xu and Y. Ma, *J. Mater. Chem. A*, 2014, **2**, 19726–19732.
65 K. Chi, Z. Zhang, J. Xi, Y. Huang, F. Xiao, S. Wang and Y. Liu, *ACS Appl. Mater. Interfaces*, 2014, **6**, 16312–16319.
66 P. Yu, X. Zhao, Z. Huang, Y. Li and Q. Zhang, *J. Mater. Chem. A*, 2014, **2**, 14413–14420.